Mechanical characterization of arterial walls based on IVUS studies

Gonzalo Daniel Maso Talou

Pablo Javier Blanco

gonzalot@lncc.br

pjblanco@lncc.br

Laboratório Nacional de Computação Científica

Av. Getúlio Vargas 333, 25651-075, RJ, Brasil

Cristiano Guedes Bezerra

Pedro Alves Lemos

cristiano.bezerra@incor.usp.br

pedro.lemos@incor.usp.br

Instituto do Coração, Hospital das Clínicas, Faculdade de Medicina, Universidade de São Paulo

Av. Dr. Enéas de Carvalho Aguiar 44, 05403-900, SP, Brasil

Raúl Antonino Feijóo

feij@lncc.br

Laboratório Nacional de Computação Científica

Av. Getúlio Vargas 333, 25651-075, RJ, Brasil

Abstract. *The understanding of the genesis, development and progression of cardiovascular diseases is key for effective diagnosis, treatment and surgical risk assessment. Notorious advances have been performed in the histological characterization of culprit plaque, although the development of strategies for the mechanical characterization of plaque and healthy tissue is an active area of research yet in its early stages. This work proposes a methodology to construct patient-specific mechanical models of the arterial wall using in-vivo data extracted from an IVUS study. Firstly, an image processing stage of the IVUS study delivers the displacement field for a particular vessel cross-section along the cardiac cycle. Then, a geometric model of the cross-section is constructed by manual segmentation of a diastolic image at the site. This model is then discretized with a finite element method to obtain a patient-specific mechanical model. Using the displacement field as observations, a reduced-order unscented Kalman filter*

is employed to estimate the constitutive parameters of the model. The obtained model allows clinically relevant applications such as: tissue characterization, stress analysis of the arterial wall, among others. The integrative use of such applications in longitudinal studies is expected to reveal new insights of the plaque characteristics and behavior.

Keywords: *Data assimilation, Computational mechanics, IVUS*

1 Introduction

Cardiovascular diseases are the principal cause of death and morbidity worldwide [1]. The two principal causes of death, cardiac ischemia and stroke, are intrinsically related with the atherosclerotic plaque development and destabilization processes, which are still largely unknown [2, 3]. At the final stage of the destabilization process, the plaque ruptures releasing thrombotic components into the blood flow which in turn generate thrombi that block the blood vessel lumen leading to the aforementioned conditions. Thus, the prediction of these ruptures and the identification of the so called culprit plaques is of extreme importance for diagnosis. The use of computational fluid-structure simulations allows not only to study the mechanical state of the vessel wall that may compromise its integrity and produce the rupture, but also, it allows to simulate different patient conditions (hypertension, hyperemia, exercise) and therapeutic procedures (angioplastic balloon inflation, stent deployment, stent-plaque interaction, among others) which are valuable resources for diagnosis, treatment and surgical risk assessment. In order to perform such simulations two inputs are required: i) the constitutive parameters of the vessel tissues and ii) the loads applied to the vessel wall.

IVUS imaging technique provides high temporal and spatial resolution of the vessel wall during the cardiac cycle. This offers a detailed in-vivo description of the vessel kinematics which can be used to infer its constitutive parameters for a given mechanical model. Some works [4, 5] have successfully classified the materials in few discrete categories (e.g. necrotic core, fibrotic, fibro-fatty or lipid-pool, calcified) labeled based on the acoustic impedance response of the tissues in a determined frame of the study. Although due to the variability of the constitutive parameters along such categories [6, 7], this information is not accurate enough for simulation purposes. Alternatively, the temporal resolution of the IVUS study can be exploited to derive the displacement field of the vessel wall along the cardiac cycle (for example, optical flow techniques or large deformation diffeomorphic metric mapping can be used). Using the displacement field as input, data assimilation techniques can be employed to estimate the constitutive parameters.

Data assimilation techniques use measurable quantities (observations) to adjust a given model such that it predicts the observations. In this scenario, the in-vivo displacements of the vessel wall are used to estimate the constitutive parameters of the vessel physical model. These techniques permit not only to derive specific quantities or constituents, but to study the physical phenomena of the scenario and, even, modify the scenario itself (e.g. simulation of therapeutic procedures or risk scenarios). In turn, measurement errors can be filtered by the physical model being a *quid pro quo* benefit: the measurements instantiate the model and the model filters the measurements. Particularly, the so called filtering approaches (also known as filtering methods) are naturally less computationally demanding when compared against other data assimilation techniques such as variational approaches [8]. Also, these methods are embarrassingly parallel which is one of the main appealing factors. Given a set of observations for our model of interest, the method makes a prediction for each observation and, then, corrects it based on the discrepancies between the model estimation and the observed data. For each prediction-correction step, several variations of the parameters are tested in order to perform a suitable correction based on the prediction statistics. Several methods based on the Kalman filter have been developed to deal with linear and non-linear dynamic problems. In [9, 10, 11] a non-linear extended Kalman filter (EKF) with collocation feedback is applied to identify the Young modulus of different regions of a heart model. A more efficient variation of these methods was

presented in [12] with a reduced order Kalman filter based on the unscented transform (abbreviated as ROUKF). This new approach does not require neither linearization nor tangent operator of the non-linear model, which eases its implementation. Interestingly, the ROUKF features a higher order approximation of the system states statistics delivering more accurate outcomes than EKF. In [8, 13, 14], ROUKF was successfully applied for estimation of Young modulus and wall thickness in arteries with tests in-vivo, in-vitro and in-silico, showing a simpler and more efficient implementation than EKF.

In this work, we present a novel methodology to construct patient-specific mechanical models of the arterial wall using in-vivo data from an IVUS study. From the IVUS study, a frame of interest is selected and the corresponding arterial wall is segmented to construct a finite element mesh. For the mechanical model, it is assumed that the lesion tissues behave as isotropic Neo-Hookean materials and that the artery is internally loaded by the blood pressure and axially stretched at all cardiac phases. Using gating, registration and optical flow methods developed in previous works [15, 16, 17], the displacement field of the vessel wall is computed along the cardiac cycle. Then, a data assimilation stage is performed where the given displacement field (computed optical flow) are the observations and the mechanical constitutive parameter are the parameters to estimate. For data assimilation, the reduced order unscented Kalman filter (ROUKF) is applied.

The manuscript is structured as follows. In Section 2, the arterial wall mechanical model is introduced (Section 2.1), followed by the patient-specific considerations for the model instantiation (Section 2.2) and, lastly, the data assimilation scheme for the estimation of the constitutive parameters of the mechanical model (Section 2.3). In Section 3, the mechanical characterization is preformed for two cases: an idealized artery and an more realistic artery constructed from an in-vivo geometry. In Section 4, the final remarks are outlined.

2 Methods

This section is divided in three parts: i) the introduction of the mechanical model for the arterial wall; ii) the patient-specific tailoring for such model; and iii) the data assimilation process to estimate the constitutive parameters of the model. The mechanical models presented in this work were developed in [18]. Particularly, a simplified version of the model which considers a pre-stretched and preloaded state of the vessel is used.

2.1 Mechanical setup for the arterial wall

Let us consider the domain of a vessel cross-sectional slice as a body described in the Euclidean space by its *spatial* configuration denoted by Ω_s with boundary $\partial\Omega_s = \partial\Omega_s^W \cup \partial\Omega_s^E \cup \partial\Omega_s^A$, where $\partial\Omega_s^W$ is the interface between the vessel and the blood, $\partial\Omega_s^E$ is the external surface, and $\partial\Omega_s^A = \bigcup_{i=1}^{2} \partial\Omega_s^{A,i}$ are the set of 2 cross-sectional (non-physical) boundaries at the axial extremes of a vessel slice (see Figure 1). The coordinates at the spatial configuration are denoted by $\mathbf{x}_s$. A *material* configuration, used as a reference configuration, is denoted by Ω_m with coordinates $\mathbf{x}_m$. In the context of hemodynamics, Ω_s stands for the configuration at which mechanical equilibrium is achieved for a given load condition (diastolic, systolic or any other loaded state of the arterial wall). Residual stresses are neglected and a load- and stress-free state is assumed at the material configuration.

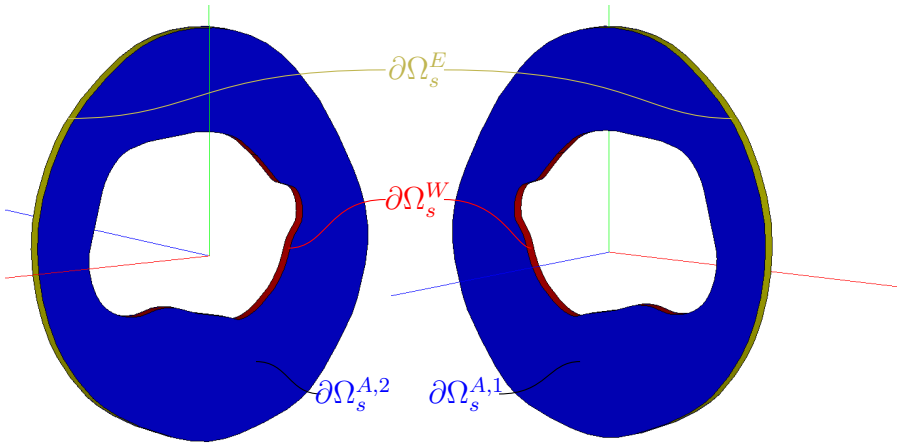

Figure 1: Spatial configuration of the vessel cross-sectional slice Ω_s and its boundaries $\partial\Omega_s = \partial\Omega_s^W \cup \partial\Omega_s^E \cup \partial\Omega_s^A$.

The displacement field from the reference to the spatial configuration is denoted by $\mathbf{u}$. Then, the deformation mapping from Ω_m onto Ω_s and its inverse are characterized by the following expressions,

$$\mathbf{x}_s = \chi_m\left(\mathbf{x}_m\right) = \mathbf{x}_m + \mathbf{u}_m, \tag{1}$$
$$\mathbf{x}_m = \chi_s\left(\mathbf{x}_s\right) = \chi_m^{-1}\left(\mathbf{x}_s\right) = \mathbf{x}_s - \mathbf{u}_s, \tag{2}$$

where subscripts m and s denote the descriptions of the fields in the material and spatial configurations, respectively. Thus, the displacement vector field is given by

$$\mathbf{u}_s(\mathbf{x}_s) = \left(\mathbf{u}_m(\mathbf{x}_m)\right)_s = \mathbf{u}_m\left(\chi_m^{-1}\left(\mathbf{x}_s\right)\right). \tag{3}$$

and the gradients of the deformation mappings are obtained as

$$\mathbf{F}_m = \nabla_m \chi_m = \mathbf{I} + \nabla_m \mathbf{u}_m, \tag{4}$$
$$\mathbf{f}_s = \nabla_s \chi_s = \nabla_s \chi_m^{-1} = \mathbf{I} - \nabla_s \mathbf{u}_s, \tag{5}$$

where ∇_m and ∇_s denote the gradients with respect to material and spatial coordinates, respectively. Observe that $[\mathbf{F}_m^{-1}]_s = \mathbf{f}_s$ and $[\mathbf{f}_s^{-1}]_m = \mathbf{F}_m$.

Further, biological tissues are assumed to behave as incompressible materials, which is mathematically represented by the following kinematic constraint

$$\det \mathbf{F}_m = 1. \tag{6}$$

In a general case the load state of the arterial cross-section can be characterized as follows: a Neumann boundary condition given by the forces exerted by the blood flow over $\partial\Omega_s^W$, i.e. a traction $\mathbf{t}_s^W$, and by the tethering tractions $\mathbf{t}_s^{A,i}$ acting over $\partial\Omega_s^{A,i}$, $i = 1, 2$. Equivalently, the tethering tractions are grouped into $\mathbf{t}_s^A$, which is defined over the whole $\partial\Omega_s^A$. We consider that no load from external tissues $\mathbf{t}_s^E = 0$ is acting on the external surface $\partial\Omega_s^E$. It is important to recall that the traction due to hemodynamic forces $\mathbf{t}_s^W$ constitutes a follower load, and can be split into normal and tangential components by $\mathbf{t}_s^W = t_s^{W,n}\mathbf{n}_s + \mathbf{t}_s^{W,t}$ where $t_s^{W,n} = \mathbf{t}_s^W \cdot \mathbf{n}_s$ is the normal component of the traction and $\mathbf{t}_s^{W,t}$ is the tangent vector which can be obtained

as $\mathbf{t}_s^{W,t} = \mathbf{P}_s \mathbf{t}_s^W$, with $\mathbf{P}_s = (\mathbf{I} - \mathbf{n}_s \otimes \mathbf{n}_s)$ being the projection operator to the plane with unit normal vector $\mathbf{n}_s$. For the application presented in this work, the tangent contribution is considered to be $\mathbf{t}_s^{W,t} = 0$, hence disregarding the shear forces imprinted by the blood flow on the vessel wall.

The mechanical problem in variational form is presented considering the incompressibility as an additional constraint. Then, an independent variable (the pressure in the solid domain) emerges as a Lagrange multiplier to accommodate this kinematic constraint.

Next, we provide the statement of two variational formulations of mechanical equilibrium which are required for the problem addressed in the present work, and whose difference is rather subtle: the known domain. In the so-called *preload problem*, the given domain is the domain at which the body is at equilibrium (the spatial domain), and the unknown domain is the reference domain used to define the constitutive equations (the material domain). In the so-called *forward problem*, the given domain is the material domain, while the unknown data is the spatial domain. Further details regarding linearization and numerical schemes for these two problems can be found in [19, 18].

Preload problem

Given the equilibrium configuration Ω_s and the load acting on the spatial configuration, the variational equations that govern this problem are those corresponding to the mechanical equilibrium expressed in the *spatial* domain. Hence, the problem reads: given the loads $\mathbf{t}_s^{W,n}$ and $\mathbf{t}_s^A$, find $(\mathbf{u}_s, \lambda_s) \in \mathcal{U}_s \times \mathcal{L}_s$ such that $\boldsymbol{\sigma}_s$ satisfies

$$\int_{\Omega_s} \left[-\lambda_s \operatorname{div} \hat{\mathbf{u}}_s + \boldsymbol{\sigma}_s \cdot \boldsymbol{\varepsilon}_s\left(\hat{\mathbf{u}}_s\right)\right] d\Omega_s = \int_{\partial\Omega_s^W} t_s^{W,n} \mathbf{n}_s \cdot \hat{\mathbf{u}}_s \, d\partial\Omega_s^W + \sum_{i=1}^{2} \int_{\partial\Omega_s^{A,i}} \mathbf{t}_s^{A,i} \cdot \hat{\mathbf{u}}_s \, d\partial\Omega_s^{A,i} \qquad \forall \hat{\mathbf{u}}_s \in \mathcal{V}_s, \quad (7)$$

$$\int_{\Omega_s} [1 - \det \mathbf{F}_s^{-1}] \hat{\lambda}_s \, d\Omega_s = 0 \quad \forall \hat{\lambda}_s \in \mathcal{L}_s, \quad (8)$$

where $\boldsymbol{\varepsilon}_s(\hat{\mathbf{u}}) = \frac{1}{2}(\nabla_s \hat{\mathbf{u}} + \nabla_s \hat{\mathbf{u}}^T)$ is the strain rate tensor in the *spatial* configuration, $\mathcal{L}_s = L^2(\Omega_s)$ and $\mathcal{U}_s = \{\mathbf{u}_s \in \mathbf{H}^1(\Omega_s),\ \mathbf{u}_s \text{ satisfies essential b.c.}\}$ are, respectively, the linear space for the Lagrange multiplier and the linear manifold associated to kinematically admissible displacements, and $\mathcal{V}_s = \left\{\hat{\mathbf{u}}_s \in \mathbf{H}^1(\Omega_s),\ \hat{\mathbf{u}}_s \text{ satisfies homogeneous essential b.c.}\right\}$ is the space of kinematically admissible variations. Also, the Cauchy stress tensor, $\boldsymbol{\sigma}_s$, is related to the second Piola-Kirchhoff stress tensor $\mathbf{S}_m$ through

$$\boldsymbol{\sigma}_s = \frac{1}{\det \mathbf{F}_s} \mathbf{F}_s (\mathbf{S}_m(\mathbf{E}_m))_s \mathbf{F}_s^T. \quad (9)$$

where the Piola-Kirchhoff stress tensor is a function of the Green-Lagrange deformation tensor $\mathbf{E}_m = \frac{1}{2}\left(\mathbf{F}_m^T \mathbf{F}_m - \mathbf{I}\right)$ via a constitutive equation of the material.

Particularly if the material does not present orthogonal fiber families of collagen (i.e. materials at the intima such as fibrotic, lipidic or calcified tissue), the constitutive equation is

considered to be derived from a strain energy function such as

$$\psi = \frac{c}{2}(I_1 - 3) \tag{10}$$

where c is the material parameter that characterizes the stiffness of the material and I_1 is the first invariant of the Cauchy-Green tensor, i.e.,

$$I_1 = \text{tr}(\mathbf{C}_m) \tag{11}$$

with $\mathbf{C}_m = \mathbf{F}_m^T \mathbf{F}_m$. Using the strain energy function, we finally obtain the material description of the second Piola-Kirchhoff stress tensor (and $\boldsymbol{\sigma}_m$ through (9)) as

$$\mathbf{S}_m(\mathbf{E}_m) = \frac{\partial \psi}{\partial \mathbf{E}_m}. \tag{12}$$

In the case that the material presents orthogonal fiber families of collagen (i.e. tissues in the tunica media and adventitia), the strain energy function is modified as proposed in [20], i.e.,

$$\psi = \frac{c}{2}(I_1 - 3) + \frac{k_1}{2\,k_2} \sum_{i=4,6} \delta_i \Big(e^{k_2[(1-\rho)(I_1-3)^2 + \rho\,(I_i - \lambda_i^0)^2]} - 1 \Big) \tag{13}$$

being

$$\delta_i = \begin{cases} 1 & I_i > \lambda_i^0 \\ 0 & \text{otherwise} \end{cases}, \tag{14}$$

$$I_i = \mathbf{a}_i \cdot (\mathbf{C}_m \mathbf{a}_i), \quad i = 4, 6, \tag{15}$$

where k_1 and k_2 characterize the stiffness of the collagen fibers, λ_i^0 is the recruitment stretch (set to 1 unless stated otherwise), $\rho \in [0, 1]$ is the mixture parameter between isotropic and anisotropic behavior of the fiber families and $\mathbf{a}_i,\ i = 4, 6$ are the vectors that indicate the orientation of the fibers at the material configuration.

Forward problem

When the material (load- and stress-free) configuration Ω_m is known, the variational equations (7)-(8) can be evaluated in terms of this reference domain, yielding what we define as the *forward problem*. In fact, the variational equations that govern the equilibrium problem expressed now in the *material* domain Ω_m are written as follows: given the material description of the loads, $\mathbf{t}_m^{W,n}$ and $\mathbf{t}_m^{A,i}$, find $(\mathbf{u}_m, \lambda_m)$ in $\mathcal{U}_m \times \mathcal{L}_m$ such that

$$\begin{aligned} &- \int_{\Omega_m} \lambda_m \left(\mathbf{F}_m^{-T} \cdot \nabla_m \hat{\mathbf{u}}_m \right) \det \mathbf{F}_m \, d\Omega_m + \int_{\Omega_m} \left(\mathbf{S}_m(\mathbf{E}_m) \right) \cdot \dot{\mathbf{E}} \left(\hat{\mathbf{u}}_m \right) \, d\Omega_m = \\ &\int_{\partial\Omega_m^W} \left(\mathbf{t}_m^{W,n} \mathbf{F}_m^{-T} \mathbf{n}_0^W \cdot \hat{\mathbf{u}}_m \right) \det \mathbf{F}_m \, d\partial\Omega_m^W \\ &\qquad + \sum_{i=1}^{2} \int_{\partial\Omega_m^{A,i}} \left(\mathbf{t}_m^{A,i} \cdot \hat{\mathbf{u}}_m \right) |\mathbf{F}_m^{-T} \mathbf{n}_0^{A,i}| \det \mathbf{F}_m \, d\partial\Omega_m^{A,i} \qquad \forall \hat{\mathbf{u}}_m \in \mathcal{V}_m, \end{aligned} \tag{16}$$

$$\int_{\Omega_m} (\det \mathbf{F}_m - 1)\hat{\lambda}_m \, d\Omega_m = 0 \quad \forall \hat{\lambda}_m \in \mathcal{L}_m, \tag{17}$$

where $\dot{\mathbf{E}}(\hat{\mathbf{u}}_m) = \frac{1}{2}[\mathbf{F}_m^T(\nabla_m \hat{\mathbf{u}}_m) + (\nabla_m \hat{\mathbf{u}}_m)^T \mathbf{F}_m]$, $\mathbf{n}_0$ is the unit normal vector in the material configuration and $\mathcal{U}_m$,$\mathcal{V}_m$ and $\mathcal{L}_m$ are the counterparts of $\mathcal{U}_s$,$\mathcal{V}_s$ and $\mathcal{L}_s$, respectively, with functions defined in Ω_m.

We emphasize that the inertial term could be easily incorporated in the solid problem. However, for coronary arteries the stresses associated to inertial forces can be safely neglected as shown in [18].

The preloaded forward problem

The *preload problem* stated above is a mandatory step towards characterizing the mechanical state, i.e. the stress state, of the arterial wall in a, for instance, geometry obtained from medical images (e.g. the end-diastolic geometry) with a given baseline hemodynamics loads (e.g. the end-diastolic pressure). The material configuration is required because it is used to define constitutive equations, without which the forward problem cannot be properly formulated. In our case, such baseline geometry is obtained from IVUS study, while the baseline hemodynamics loads (the blood pressure) are estimated from patient specific data. Just after solving the preload problem, the baseline mechanical state, that is the stress state due to the preload pressure (i.e. pressure at diastole), is determined and the *forward problem* can be solved to determine the equilibrium configuration for other hemodynamics loads occurring during the cardiac cycle. In that manner both problems are sequentially coupled to solve a forward problem from an adequately preloaded configuration.

Note that, given a set of loads for the vessel, the preload problem is solved only once and, then, the *forward problem* is solved for different levels of load.

2.2 Patient-specific mechanical model

Using IVUS studies, we derive a geometrical model for a frame of interest (see Figure 2). Firstly, the intima-media area is manually segmented from the image using cubic splines. The segmented surface is extruded 0.1mm in the axial vessel direction. Then, the volume is divided in media and intima tunica, where the media has homogeneous thickness and is the outer layer. An adventitia layer of $300 - 500\mu$m thickness is added as an outer layer. If further materials must be detailed in the lumen (for example calcium inclusions, lipid pool areas), we employ the CAD tools in the software Salome 7.8.0 to split the corresponding volumes. The resulting volume is meshed using Netgen 1D-2D-3D embedded in Salome 7.8.0 software and, also, groups of elements, faces and nodes are created to define their constraints and constitutive parameters. The obtained mesh is finally exported in UNV format to our in-house numerical solver.

2.3 Data assimilation

For the data assimilation process, the following is assumed to be known: i) the domain partition $\Omega_s = \bigcup_{i=1}^{R} \Omega_s^i$ of R disjoint regions with their own homogeneous constitutive parameters; ii) the loads $\mathbf{t}_s^{W,n}$ (obtained by medical instrumentation); and iii) the approximated displacement

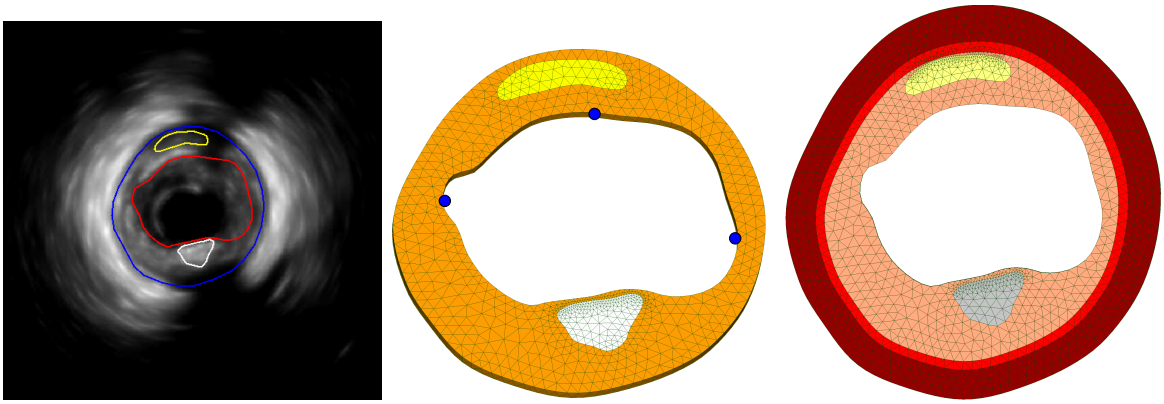

Figure 2: Pipeline for geometric model generation: (left) segmentation of the intima-media, calcified tissue and a proposed lipid pool area over the IVUS image; (middle) extruded volume of the of the segmented surfaces and selection of nodes with orthogonal displacements constraint (blue dots); (right) separation of the tunica intima and media and addition of the adventitia. The final mesh features the adventitia (dark-red), media (red), fibrotic tissue (light-orange), lipidic tissue (light-yellow) and calcified tissue (gray).

fields $\mathbf{u}_s^{\mathrm{T}}$ (obtained by image processing techniques) at S different times. Since our problem is static, the time instants in the context of the Kalman filter correspond to the different load levels. Hereafter we refer simply to time instants, but the association with the load level must be kept in mind. By using the mechanical models presented in the previous section, we want to estimate the constitutive parameters such that

$$\theta = \arg\min_{\hat{\theta}} \sum_{s=1}^{S} \|\mathbf{u}_s^{\mathrm{M}}(\hat{\theta}) - \mathbf{u}_s^{\mathrm{T}}\|_{L_2}^2 \tag{18}$$

where $\mathbf{u}_s^{\mathrm{M}}(\hat{\theta})$ is the displacement field at the time s obtained by solving the preload and forward problems (described in Section 2.1) with the constitutive parameters $\hat{\theta}$.

This parameter identification problem can be rewritten as the discrete dynamic nonlinear system presented as follows

$$\begin{aligned} X_k^a &= f(X_{k-1}^a, t_{k-1}) + W_k \\ Z_k &= h(X_k, t_k) + V_k \end{aligned} \tag{19}$$

where X_k is the augmented state vector

$$X_k^a = [\mathbf{u}_{t_k}(x_1), \ldots, \mathbf{u}_{t_k}(x_N), \lambda_{t_k}(x_1), \ldots, \lambda_{t_k}(x_N), \theta_1, \ldots, \theta_M]^T \tag{20}$$

that contains the displacement $\mathbf{u}_{t_k}$ and pressure λ_{t_k} fields at N points along the vessel wall, and the M constitutive parameters of all regions of the domain; $f(X_k^a, t_k)$ is the operator that sequentially solves the preload and forward problem for the given parameters in X_k at the time t_k; W_k are the model errors at the k-th step; $h(X_k^a, t_k) = \mathbf{H}X_k^a$ is a linear operator represented by the block matrix

$$\mathbf{H} = \begin{bmatrix} \mathbf{I}_{N\times N} & \mathbf{0}_{N\times(N+M)} \\ \mathbf{0}_{(N+M)\times N} & \mathbf{0}_{(N+M)\times(N+M)} \end{bmatrix} \tag{21}$$

where $\mathbf{I}$ is the identity matrix and the sub-indexes of the matrices indicate their size as rows by columns; Z_k is the image processing observation described by the column vector

$$Z_k = [\tilde{\mathbf{u}}_{t_k}^{\mathrm{T}}(x_1), \ldots, \tilde{\mathbf{u}}_{t_k}^{\mathrm{T}}(x_N), \mathbf{0}_{N+M}]^T \tag{22}$$

where $\tilde{\mathbf{u}}_{t_k}^{\mathrm{T}}(x_i)$ is the interpolated value at the spatial position x_i and time t_k of the displacement field given by the image processing technique.

Then, a traditional reduced order unscented Kalman filter (ROUKF) with spherical sigma-points (see [21], [22] and [23]) is applied by using the following 4-step algorithm:

1. Sigma points generation $\sigma_i^{(n)}, i = 1, \ldots, M+1$ and variables initialization

$$\begin{gathered}\mathbf{R}_0 = \sigma_{\mathrm{T}}\,\mathbf{I}; \quad \mathbf{L}_0 = \begin{bmatrix}\mathbf{0}_{2N\times M}\\ \mathbf{I}_{M\times M}\end{bmatrix}; \quad \mathbf{U}_0^{-1} = \begin{bmatrix}\sigma_{\hat{\theta}_0} & \ldots & 0\\ \vdots & \ddots & \vdots\\ 0 & \ldots & \sigma_{\hat{\theta}_M}\end{bmatrix}\\ X_0^a = [\mathbf{0}_N, 0_N, \hat{\theta}_1, \ldots, \hat{\theta}_M]^T; \quad \mathbf{P}_0^+ = \mathbf{L}_0\mathbf{U}_0^{-1}\mathbf{L}_0^T.\end{gathered} \tag{23}$$

2. The *prediction* step

$$\begin{aligned}\hat{X}_{k-1}^{(i)} &= \hat{X}_{k-1}^{+} + \mathbf{L}_{k-1}^{X}\sqrt{\mathbf{U}_{k-1}^{-1}}\,\sigma_i^{(n)}, \quad i = 1, \ldots, M+1\\ \hat{\theta}_{k-1}^{(i)} &= \hat{\theta}_{k-1}^{+} + \mathbf{L}_{k-1}^{\theta}\sqrt{\mathbf{U}_{k-1}^{-1}}\,\sigma_i^{(n)}, \quad i = 1, \ldots, M+1\\ \begin{bmatrix}(\hat{X}_k^{(i)})\\ (\hat{\theta}_k^{(i)})\end{bmatrix} &= f\Big(\begin{bmatrix}(\hat{X}_{k-1}^{(i)})\\ (\hat{\theta}_{k-1}^{(i)})\end{bmatrix}, t_{k-1}\Big)\\ \hat{X}_k^{-} &= \sum_{i=1}^{N+1} w^{(i)}\hat{X}_k^{(i)}\\ \hat{\theta}_k^{-} &= \sum_{i=1}^{N+1} w^{(i)}\hat{\theta}_k^{(i)}.\end{aligned} \tag{24}$$

3. The *correction* step

$$\begin{aligned}\mathbf{L}_k^X &= \hat{\mathbf{X}}_k^{(*)}\mathbf{D}_w(\boldsymbol{\sigma}^{(*)})^T\\ \mathbf{L}_k^\theta &= \hat{\boldsymbol{\theta}}_k^{(*)}\mathbf{D}_w(\boldsymbol{\sigma}^{(*)})^T\\ \{\mathbf{HL}\}_k &= \hat{\mathbf{Z}}_k^{(*)}\mathbf{D}_w(\boldsymbol{\sigma}^{(*)})^T\\ \mathbf{U}_k &= \mathbf{P}_w + \{\mathbf{HL}\}_k^T\mathbf{R}_k^{-1}\{\mathbf{HL}\}_k\\ \hat{X}_k^{+} &= \hat{X}_k^{-} + \mathbf{L}_k^X\mathbf{U}_k^{-1}\{\mathbf{HL}\}_k^T\mathbf{R}_k^{-1}\Big(Z_k - \sum_{i=1}^{M+1} w^{(i)}\hat{Z}_k^{(i)}\Big)\\ \hat{\theta}_k^{+} &= \hat{\theta}_k^{-} + \mathbf{L}_k^\theta\mathbf{U}_k^{-1}\{\mathbf{HL}\}_k^T\mathbf{R}_k^{-1}\Big(Z_k - \sum_{i=1}^{M+1} w^{(i)}\hat{Z}_k^{(i)}\Big).\end{aligned} \tag{25}$$

The matrices $\boldsymbol{\sigma}^{(*)}, \hat{\mathbf{X}}_k^{(*)}, \hat{\mathbf{Z}}_k^{(*)}, \hat{\boldsymbol{\theta}}_k^{(*)}$ are the $M \times (M+1)$ matrices whose columns are the vectors $\sigma^{(i)}, \hat{X}_k^{(i)}, \hat{Z}_k^{(i)}, \hat{\theta}_k^{(i)}$ with $i = 1, \ldots, M+1$, respectively. $\mathbf{D}_w$ is the diagonal $(M+1) \times (M+1)$ matrix with values $D_{ii} = w_i, i = 1, \ldots, M+1$, i.e., the sigma-point weights.

4. If stop criteria is not achieved, go to step 2.

The initial guess for the parameters $\hat{\theta}_i$ and their uncertainties $\sigma_{\hat{\theta}_i}$ are reported in Section 3 for each case.

3 Results

We study two cases with increasing complexity of the model:

1. **Synthetic idealized artery**: We assume an ideal geometry of an arterial cross section with two concentric layers, modeling the media/adventitia and the intima layer, respectively. An in-silico displacement field is obtained by solving the preload and forward problems. Using such displacements as observations for the ROUKF, we analyze: i) the impact of alternative media/adventitia models; and ii) the capabilities of the ROUKF method to identify the constitutive parameters for different homogeneous intimal tissues.
2. **Synthetic artery with in-vivo geometry**: We segment the media and intima from an IVUS image to obtain a realistic arterial domain. There, we define a distribution of tissues within the vessel wall and, as before, we create an in-silico displacement field solving the preload and forward problems. Finally, the constitutive parameters were estimated with the proposed method in normotensive and hypertensive scenarios. In these scenarios, we analyze the capabilities to estimate the constitutive parameters in real geometries with heterogeneous composition (although the tissue distribution is synthetic) under physiological ranges of pressure.

3.1 Synthetic idealized artery

The idealized artery is a perfect ring with inner and outer radii of 2mm and 2.55mm, and an axial thickness of 0.04mm. The domain is split in two concentric layers, the inner layer with a radial thickness of 0.2mm models the intima while the outer layer with a radial thickness of 0.35mm models the media and adventitia. Loads of $\mathbf{t}^{W,n} = 80\,\mathbf{n}$ mmHg and $\mathbf{t}^{W,n} = 120\,\mathbf{n}$ mmHg are applied in the inner surface for the preload and forward problem, respectively, simulating a normotensive scenario and tethering tractions $\mathbf{t}_s^{A,i}$ such that an axial stretch of 10% is imposed in the axial direction. Due to the intrinsic symmetry of the problem, we solve only a quarter of the domain (see Figure 3). Two non-physical boundaries appear as result of this simplification where homogeneous Dirichlet conditions are imposed to allow only radial displacements.

This idealized geometry is used to test the sensitivity of the estimation of material behavior of tissues in the intimal layers when inaccurate adventitia models are used. The reason for this study is because the data for the adventitia is insufficient for its parameter estimation (the external boundary is are not clearly delineated in the IVUS images), thus it is of interest to assess the error in the estimation of material properties in the intima when softer or stiffer adventitia models are used. Additionally, it is also studied the use of an adventitia model where

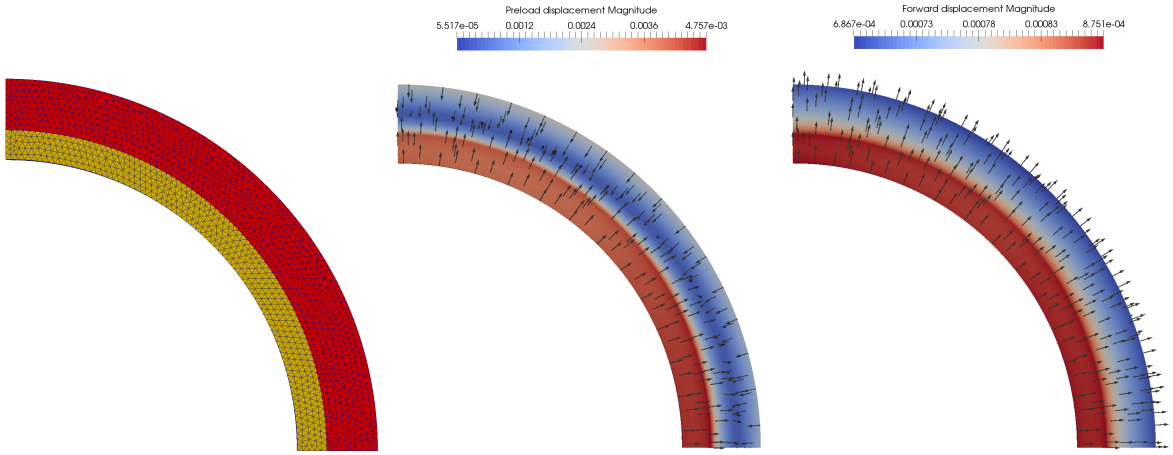

Figure 3: Domain discretization for the synthetic idealized artery and in-silico generated displacement fields for the soft media/adventitia model with an homogeneous intimal tissue with $c = 4000$ kPa (calcified tissue). (Left) Domain discretization used for the FEM numerical scheme, the intima and media/adventitia are the yellow and red elements, respectively; (middle) displacements obtained from the preload problem (in cm); (right) displacements obtained from the forward problem (in cm). Recall that the vessel is axially stretched by 10% in the configuration Ω_s, then the displacements obtained from the preload problem present an axial component besides the cross-sectional components of displacement.

Adventitia model	c (kPa)	k_1 (kPa)	k_2	θ	ρ	λ_0
Soft	4.5	37.06	48.36	65.8	0.4	1
Stiff	29.86	119.25	213.81	53.4	0.6	1
Optimized	–	–	213.81	53.4	0.6	1

Table 1: Experimental coefficients reported in [24] for patients VIII (soft model) and X (stiff and optimized model). The optimized model referred to the stiff model where parameters c and k_1 are optimized by the reduced order unscented Kalman filter.

its parameters c and k_1 are optimized along the data assimilation process. To be fair with these soft and stiff models (see the parameters in Table 1), the in-silico displacements are generated with adventitia coefficients $c = 15.8$ kPa, $k_1 = 25.36$ kPa, $k_2 = 67.85$, $\theta = 70.3°$ and $\rho = 0.7$, which represent a middle-term between the two models. These coefficients were taken from ex-vivo specimens to ensure physiological behavior of the materials (see [24], Patient VIII, Patient VI and Patient X for the soft, middle-term and stiff). Using such outer layer, three experiments were created each one with a different intimal tissue: a fibrotic tissue with $c = 500$ kPa; a lipidic tissue with $c = 100$ kPa; and a calcified tissue with $c = 4000$ kPa. Thus, we estimate the parameters of the intimal tissue using only the in-silico displacements on the intima (data that can potentially and reliably be extracted from IVUS). The main focus is to analyze the error in the estimate when using a stiffer, a softer or an optimized model for the adventitia. This allows to determine a range of confidence for the estimates made with each model when the adventitia coefficients are unknown.

The ROUKF estimation was performed using each of the three adventitia models for each

Intimal tissue	Adventitia model	2^{θ^t} (kPa)	$2^{\hat{\theta}}$ (kPa) Estimation	[LB,UB])	ε_c (%)
Fibrotic	Soft	500	598.85	$[302.21, 1186.68]$	19.77%
Lipidic	Soft	100	179.86	$[90.58, 357.16]$	79.86%
Calcified	Soft	4000	3915.23	$[1965.72, 7798.16]$	2.12%
Fibrotic	Stiff	500	456.60	$[230.36, 905.05]$	8.68%
Lipidic	Stiff	100	56.88	$[28.622, 113.043]$	43.12%
Calcified	Stiff	4000	3327.88	$[1672.70, 6620.89]$	16.80%
Fibrotic	Optimized	500	632.42	$[316.35, 1264.29]$	26.48%
Lipidic	Optimized	100	102.98	$[51.51, 105.88]$	2.98%
Calcified	Optimized	4000	3937.52	$[1984.28, 7813.46]$	1.56%

Table 2: Estimate of intimal tissues using the soft, stiff and optimized models for the adventitia layer. The optimized model estimates the coefficients c and k_1 of the adventitia layer using reduced order unscented Kalman filter. The estimate $2^{\hat{\theta}}$ of the true parameter 2^{θ^t} is presented with its uncertainty interval [LB,UB] $= \left[2^{\hat{\theta}-\sqrt{\mathbf{diag}(\mathbf{U}^{-1})}}; 2^{\hat{\theta}+\sqrt{\mathbf{diag}(\mathbf{U}^{-1})}}\right]$. The relative error of the elasticity modulus is computed as $\varepsilon_c = (|2^{\theta^t} - 2^{\hat{\theta}}|)/2^{\theta^t}$. The observed displacement Z are generated using a adventitia model with coefficients $c = 15.8$ kPa, $k_1 = 25.36$ kPa, $k_2 = 67.85$, $\theta = 70.3°$ and $\rho = 0.7$ (which is elastically a middle term between the soft and stiff models). The Kalman parameters for uncertainty were $\sigma_Z = 10^{-3}$ and $\sigma_\theta = 4$.

of the three intimal tissue experiments. The error in terms of the c parameter, ε_c, (see Table 2) indicates that the best estimation for fibrotic tissue is obtained by the stiff model, while for lipidic and calcified tissues it is given by the optimized model. The mean error across the three experiments are 87.83, 252.88 and 65.96 kPa for the soft, stiff and optimized models, respectively, showing a close agreement between the optimized model and soft model. The relative error of the experiments also presented the optimized model as the most accurate solution, with less than 26.48% of error for all materials. Another interesting outcome from these experiments is the fact that the uncertainty interval always comprises the correct value of c without overlapping with the c value of the other types of tissue. However, this is not enough to ensure that all the three models will perform successfully in a more realistic situation. This is because of the complexity of the geometry or the material composition (fibro-lipidic materials or small calcium inclusions on other tissue) that an in-vivo scenario may present. In fact, the next case aims to study the performance of the ROUKF estimation in a realistic arterial geometry.

3.2 Synthetic artery with in-vivo geometry

A more complex geometry extracted from an IVUS frame segmentation is now employed to assess the performance of the ROUKF on realistic vessel geometries under physiological pressure ranges. The chosen IVUS frame corresponds to a lesion with 57.4% stenosis at the end-diastolic phase. A manual demarcation of a lipid and calcified areas was performed by a specialist based on visual inspection of the image intensities. The intima/media layer obtained from the segmentation was considered as intima layer only, since the mechanical contribution of the media with presence of significant plaque and in passive conditions (no smooth muscle activation is considered) is negligible when compared to the intimal plaque contribution. The generated mesh of the domain for the numerical simulation is presented in Figure 4 where a calcified and lipid-pool regions were delineated without strict relation to the underlying in-vivo materials. The aim of this scenario is the analysis of the data assimilation procedure on a realistic media/intima geometry, for which the tissue distribution seems morphologically reasonable.

To generate the in-silico displacement field, we use the middle-term adventitia model and three neo-hookean materials without fibers (see equation (10)), a fibrotic material with $c = 500$ kPa, a lipidic material with $c = 100$ kPa and a calcified material with $c = 4000$ kPa. The same loads as in the previous section were applied for the normotensive scenario and loads of $\mathbf{t}^{W,n} = 90\,\mathbf{n}$ mmHg and $\mathbf{t}^{W,n} = 140\,\mathbf{n}$ mmHg are applied over the inner surface for the preload and forward problem for the hypertensive scenario. Tethering tractions $\mathbf{t}_s^{A,i}$ at the non-physical axial boundaries are applied such that an axial stretch of 10% is prescribed. Additionally, rigid motions is removed by constraining orthogonal displacements with respect to the boundary at 3 points over $\partial\Omega_s^W$ (see blue points in Figure 3). The ROUKF optimizes the coefficients (c, k_1) and (c) for the neo-hookean materials with and without fibers. The parameter uncertainties are 1 and 4 for the fibrous and non-fibrous materials, respectively. Such values presented a convenient balance between convergence rate and stability of the method (see [17]).

The results reported in Table 3 show that the method characterizes correctly the properties in the intimal region for the hypertensive case and only misses the calcified tissue for the normotensive case. The reason for this misidentification, is associated with the small displacement at its locus. In Figure 5, it is seen that the displacement in such region is close to 12μm in the normotensive condition and close to 16μm in the hypertensive condition. In turn, as shown in

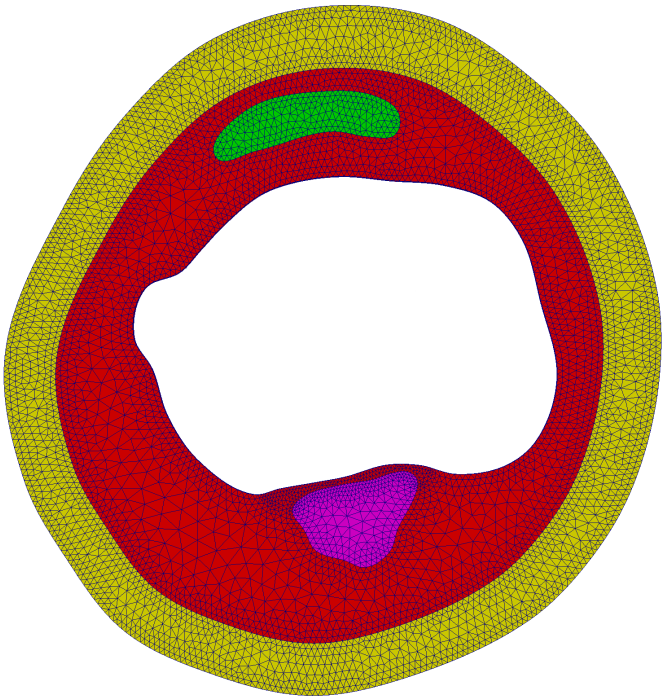

Figure 4: Domain discretization for the synthetic artery with in-vivo geometry. The intima is composed by a fibrotic (red), a lipidic (green) and calcified (magenta) partitions, enclosed by the adventitia (yellow) partition.

Figure 6, the error in such area is similar for both cases ($\approx 3\mu$m, i.e. a relative error of 25% for the normotensive case and 18.75% for the hypertensive case) degrading more the identification of the normotensive case.

With this example, it has been illustrated that the strategy based on the ROUKF delivers a successful characterization when the displacements in the materials are large enough to analyze the sensitivity of the parameters. This is an important issue to take into consideration when analyzing lesions with severe stenoses or calcified rings because such features reduce the compliance of the vessel and may lead to insufficient input data for a successful estimation.

4 Final Remarks

A data assimilation framework for the analysis of arterial models and biomechanical characterization has been presented. The in-silico experiments reported in Section 3.1 and 3.2 have shown that the methodology is capable to recover biomechanical properties of the intimal tissue when the distribution of the vessel constituents is known and the arterial pressure is large enough to cause significant deformations in the tissues.

This new tool enables several new studies targeting the in-vivo and patient-specific characterization of the vessel wall tissues, such as: development of shape optimization methods to obtain an in-vivo distribution of the vessel tissues; analysis of the axial and external stress forces along the tissue characterization; assessment of uncertainty of the optical flow observations to establish a heterogeneous distribution of the parameter σ_Z along the image.

Case	Parameter	2^{θ^t} (kPa)	$2^{\hat{\theta}}$ (kPa)		Rel. error
			Estimation	[LB,UB])	$\varepsilon_c\,(\%)$
Normotensive	Fibrotic c	500	663.86	$[332.60, 1325.04]$	32.77%
	Lipidic c	100	81.10	$[40.66, 161.76]$	18.9%
	Calcified c	4000	591.13	$[295.90, 1180.94]$	$85,22\%$
	Adventitia c	15.8	80.06	$[40.16, 159.60]$	$406,70\%$
	Adventitia k_1	25.36	59.72	$[29.91, 119.22]$	$135,49$
Hypertensive	Fibrotic c	500	641.85	$[321.51, 1281.35]$	28.37%
	Lipidic c	100	96.25	$[48.25, 191.98]$	3.75%
	Calcified c	4000	3631.12	$[1816.99, 7256.53]$	9.22%
	Adventitia c	15.8	75.12	$[37.66, 149.83]$	375.44%
	Adventitia k_1	25.36	7.18	$[3.60, 14.33]$	71.69%

Table 3: ROUKF estimate of the constitutive parameters in the case of a synthetic artery with in-vivo geometry. The estimate $2^{\hat{\theta}}$ of the true parameter 2^{θ^t} is presented with its uncertainty interval [LB,UB] $= \left[2^{\hat{\theta}-\sqrt{\mathbf{diag}(\mathbf{U^{-1}})}}; 2^{\hat{\theta}+\sqrt{\mathbf{diag}(\mathbf{U^{-1}})}}\right]$. The parameter estimate relative error is computed as $\varepsilon_c = (|2^{\theta^t} - 2^{\hat{\theta}}|)/2^{\theta^t}$. The Kalman parameters for uncertainty were $\sigma_Z = 10^{-3}$, and $\sigma_\theta = 1$ and $\sigma_\theta = 4$ for materials with and without fibers.

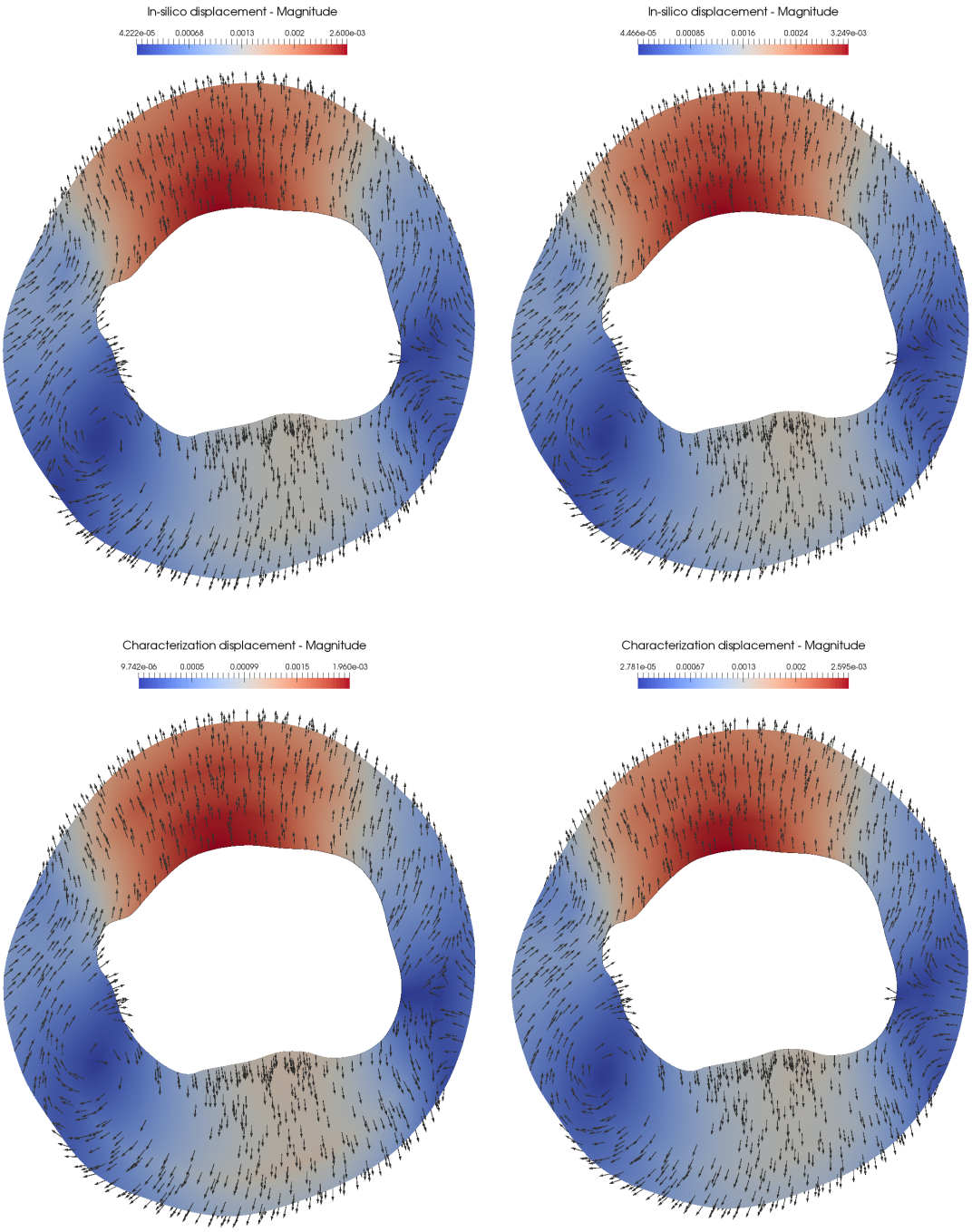

Figure 5: Comparison of the displacement field (in cm) for the forward problem obtained by in-silico experiment and as result of the data assimilation process (characterization): (first-column) normotensive case; (second-column) hypertensive case.

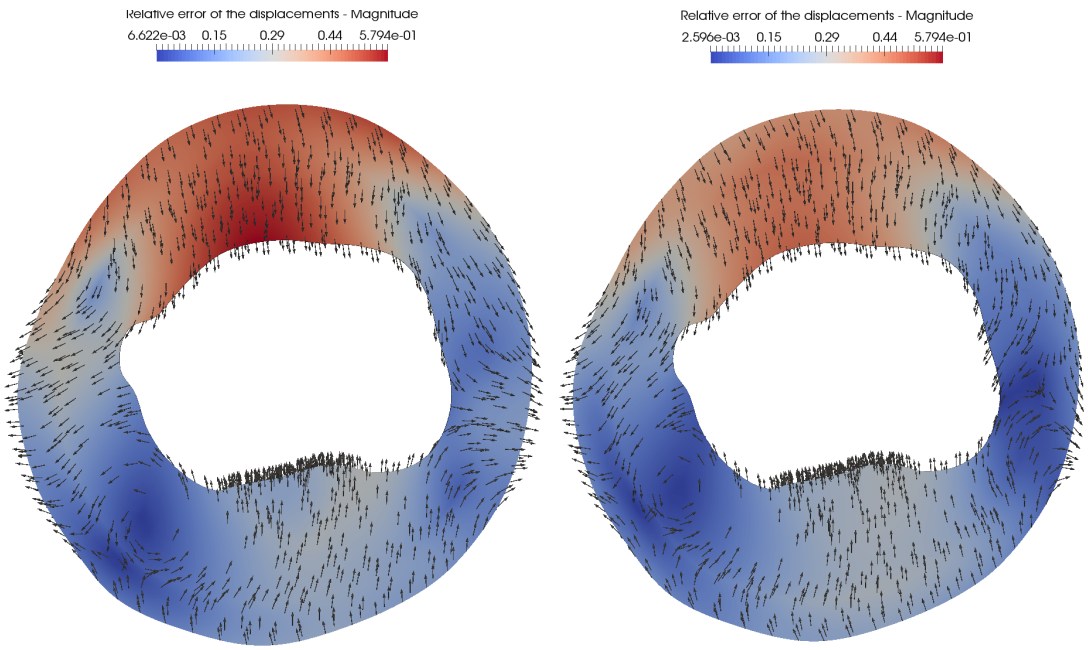

Figure 6: Error of the displacement field (in cm) for the forward problem between the in-silico experiment and the result of the data assimilation process (characterization): (left) normotensive case; (right) hypertensive case. The relative error of the displacements is computed as $\varepsilon_r = |\Omega_s| \frac{|\mathbf{u}_s^m - \mathbf{u}_s^t|}{\int_{\Omega_s} |\mathbf{u}_s^t| \mathbf{d}\Omega}$ where $\mathbf{u}_s^t$ and $\mathbf{u}_s^m$ are the in-silico and estimated displacements respectively.

5 Acknowledgements

This work was partially supported by the Brazilian agencies CNPq, FAPERJ and CAPES. The support of these agencies is gratefully acknowledged.

Bibliography

[1] Colin Mathers, Gretchen Stevens, Wahyu Retno Mahanani, Jessica Ho, Doris Ma Fat, and Dan Hogan. Who methods and data sources for country-level causes of death 2000-2015. Technical report, World Health Organization, 2016.

[2] Filippo Crea and Giovanna Liuzzo. Pathogenesis of acute coronary syndromes. *J. Am. Coll. Cardiol.*, 61(1):1–11, 2013.

[3] Jacob Fog Bentzon, Fumiyuki Otsuka, Renu Virmani, and Erling Falk. Mechanisms of plaque formation and rupture. *Circ. Res.*, 114(12):1852–1866, 2014.

[4] Anuja Nair, Barry D Kuban, E Murat Tuzcu, Paul Schoenhagen, Steven E Nissen, and D Geoffrey Vince. Coronary Plaque Classification With Intravascular Ultrasound Radiofrequency Data Analysis. *Circulation*, 106(17):2200–2206, October 2002.

[5] Shashidhar Sathyanarayana, Stéphane Carlier, Wenguang Li, and Lewis Thomas. Characterisation of atherosclerotic plaque by spectral similarity of radiofrequency intravascular ultrasound signals. *EuroIntervention*, 5(1):133–139, May 2009.

[6] Michael T Walsh, Eoghan M Cunnane, John J Mulvihill, Ali C Akyildiz, Frank J Gijsen, and Gerhard A Holzapfel. Uniaxial tensile testing approaches for characterisation of atherosclerotic plaques. *J. Biomech.*, 47(4):793–804, 2014.

[7] Howard M Loree, Alan J Grodzinsky, Susan Y Park, Lorna J Gibson, and Richard T Lee. Static circumferential tangential modulus of human atherosclerotic tissue. *J. Biomech.*, 27(2):195–204, 1994.

[8] Cristóbal Bertoglio, Philippe Moireau, and Jean-Frederic Gerbeau. Sequential parameter estimation for fluid–structure problems: Application to hemodynamics. *Int J Numer Method Biomed Eng*, 28(4):434–455, 2012.

[9] Philippe Moireau, Dominique Chapelle, and Patrick Le Tallec. Joint state and parameter estimation for distributed mechanical systems. *Comput Methods Appl Mech Eng*, 197(6):659–677, 2008.

[10] Philippe Moireau, Dominique Chapelle, and Patrick Le Tallec. Filtering for distributed mechanical systems using position measurements: perspectives in medical imaging. *Inverse Prob.*, 25(3):035010, 2009.

[11] Dominique Chapelle, Philippe Moireau, and Patrick Le Tallec. Robust filtering for joint state parameter estimation for distributed mechanical systems. *Discrete and Continuous Dynamical Systems-Series A*, 23(1-2):65–84, 2009.

[12] Philippe Moireau and Dominique Chapelle. Reduced-order unscented kalman filtering

with application to parameter identification in large-dimensional systems. *ESAIM Control Optim. Calc. Var.*, 17(2):380–405, 2011.

[13] Cristobal Bertoglio, David Barber, Nicholas Gaddum, Israel Valverde, Marcel Rutten, Philipp Beerbaum, Philippe Moireau, Rodney Hose, and Jean-Frédéric Gerbeau. Identification of artery wall stiffness: In vitro validation and in vivo results of a data assimilation procedure applied to a 3d fluid–structure interaction model. *J. Biomech.*, 47(5):1027–1034, 2014.

[14] A Caiazzo, Federica Caforio, Gino Montecinos, Lucas O Muller, Pablo J Blanco, and Eluterio F Toro. Assessment of reduced-order unscented kalman filter for parameter identification in 1-dimensional blood flow models using experimental data. *Int J Numer Method Biomed Eng*, 2017.

[15] Gonzalo D Maso Talou, Ignacio Larrabide, Pablo J Blanco, Cristiano Guedes Bezerra, Pedro A Lemos, and Raúl A Feijóo. Improving cardiac phase extraction in ivus studies by integration of gating methods. *IEEE Trans. Biomed. Eng.*, 62(12):2867 – 2877, 2015.

[16] Gonzalo D Maso Talou, Pablo J Blanco, Ignacio Larrabide, Cristiano Guedes Bezerra, Pedro A Lemos, and Raul A Feijoo. Registration methods for ivus: Transversal and longitudinal transducer motion compensation. *IEEE Trans. Biomed. Eng.*, 64(4), Apr 2016.

[17] Gonzalo D. Maso Talou. *From medical image processing to in-vivo mechanical characterization: A framework based on IVUS studies*. PhD thesis, Laboratório Nacional de Computação Científica, March 2017.

[18] Gonzalo D Ares. *Integrative Computational Modeling & In-vivo Characterization of Residual Deformations in Hemodynamics*. PhD thesis, National Laboratory for Scientific Computing, 2016.

[19] Pablo J Blanco, Gonzalo D Ares, Santiago A Urquiza, and Raúl A Feijóo. On the effect of preload and pre-stretch on hemodynamic simulations: an integrative approach. *Biomech. Model. Mechanobiol.*, 15(3):593–627, 2016.

[20] José F Rodríguez, Cristina Ruiz, Manuel Doblaré, and Gerhard A Holzapfel. Mechanical stresses in abdominal aortic aneurysms: influence of diameter, asymmetry, and material anisotropy. *J. Biomech. Eng.*, 130(2):021023, 2008.

[21] Simon J Julier and Jeffrey K Uhlmann. Reduced sigma point filters for the propagation of means and covariances through nonlinear transformations. In *Proceedings of the 2002 American Control Conference*, volume 2, pages 887–892. IEEE, 2002.

[22] Simon J Julier. The spherical simplex unscented transformation. In *American Control Conference, 2003. Proceedings of the 2003*, volume 3, pages 2430–2434. IEEE, 2003.

[23] Simon J Julier and Jeffrey K Uhlmann. Unscented filtering and nonlinear estimation. *Proceedings of the IEEE*, 92(3):401–422, 2004.

[24] Gerhard A Holzapfel, Gerhard Sommer, Christian T Gasser, and Peter Regitnig. Determination of layer-specific mechanical properties of human coronary arteries with nonatherosclerotic intimal thickening and related constitutive modeling. *Am J Physiol Heart Circ Physiol*, 289(5):H2048–H2058, 2005.